An image-based local homogenization method to model mass transport at the steel-concrete interface

Z. Zhang and U. Angst
ETH Zurich, Institute for Building Materials, Zurich, Switzerland

A. Michel and M. Jensen
Technical University of Denmark, Department of Civil Engineering, Lyngby, Denmark

ABSTRACT

Mass transport (moisture and ions) at the steel-concrete interface is closely related to corrosion of rebar in reinforced concrete structures. Thus, in the model simulating mass transport, the structure of the steel-concrete interface must be well represented. In this study, an image-based local homogenization method is proposed based on images taken in the scanning electron microscope (SEM) under the backscattered electron (BSE) detector. According to the gray level of the image, porosity can be calculated and then proposed equations are used to associate the transport properties (sorption isotherms, diffusion coefficients and permeability) with porosity. Experimental data of chloride concentration taken from the literature are used to validate the proposed method and a good agreement with simulated results them is found.

Keywords: Mass transport; Back-scattered electrons (BSE); Porosity; Local homogenization; Steel-concrete interface; Corrosion

1.0   INTRODUCTION

The degradation of reinforced concrete structures subjected to the natural environment is one of the major concerns about the durability issues. When pH in reinforced concrete decreases caused by carbonation, or when chloride penetrates into concrete with liquid water, corrosion is apt to occur at the steel-concrete interface (SCI) (Angst *et al.*, 2017). To evaluate the degradation of reinforced concrete structures, mass transport behavior at the SCI must be well understood. In this study, we are primarily interested in using numerical tools to simulate mass transport at the SCI.

SEM images show that the thickness of the SCI, including mill scale, water bleeding zone and corrosion product-filled paste, is generally smaller than 1 mm (Wong *et al.*, 2010; Zhao *et al.*, 2017). At this scale, the presence of aggregates can significantly affect the mass transport and the growth of corrosion products, and therefore the SCI cannot be viewed as a homogeneous domain. Instead, its heterogeneity has to be considered in numerical simulations.

To construct the structure for numerical modelling at the mesoscale, concrete can be separated into several individual components, such coarse aggregates, interfacial transition zone (ITZ), and mortar matrix (cement paste with fine aggregates). Coarse aggregates are commonly considered as impermeable and excluded in the simulations. The mortar matrix is treated as a homogeneous medium with a certain size of fine aggregates being assumed to uniformly distribute in cement paste. In the study of Du *et al.* (2014), all aggregates smaller than 2 mm are included in the mortar matrix. The ITZ was viewed as a uniform thin layer around each aggregate and the thickness was assigned as 500 μm which is much wider than the actual thickness of ITZ (e.g., 20 - 45 μm according to Horne *et al.* (2007)). The purpose of using a relatively large thickness is to ensure that ITZ can be properly meshed for simulations. Similarly, Abyaneh *et al.* (2013) also took the bulk mortar as a homogeneous material, by they did not use a single thickness for the ITZ. Alternatively, they set an exponential function for the porosity distribution in the ITZ showing that ITZ porosity becomes the same as the bulk porosity at about 40 μm from the aggregate. The choice of method to heterogenize the material is always dependent on the size of the domain and the resolution of the simulations. The domain size in Du *et al.* (2014) was several centimetres, so a 500 μm thick ITZ can be reasonably meshed. Abyaneh *et al.* (2013) simulated water transport in a cube of 7.5 mm and a 40 μm ITZ could be captured. They found that to consider the effect of ITZ, the voxel size must be smaller than 16.7 μm. However, these methods are much idealized because the ITZ is not uniform around the aggregate. In contrast, it is always dependent on the size of cement particles, the orientation of the aggregate and bleeding effects. In addition, the

shapes of aggregates in concrete are not the ideal sphere, ellipsoid or oblate sphere.

In this study, we follow the concept that the SCI can be viewed as a composite material. However, we do not assume whether the mortar matrix (cement paste with fine aggregates) is or not a homogeneous domain. The geometry for simulations is obtained from experimental measurements, such as SEM-BSE images. The material is divided into different phases according to the gray level of the image, such as impermeable steel, coarse aggregates with extremely low permeability and mortar consisting of cement paste and fine aggregates. At each pixel, the material is locally viewed as a homogenous mixture of pores, hydration products, anhydrous cement and fine aggregates.

This paper is organized as follows. The classical moisture and ion transport models are firstly presented, and then the method to consider the heterogeneity of the SCI is proposed. Finally, the simulated results of chloride concentration are compared with the experimental measurements by X-ray fluorescence.

2.0 CLASSICAL TRANSPORT MODELS

2.1 Moisture transport

After the casting, reinforced concrete structures are exposed to various ambient relative humidity (RH), meaning that the material is normally unsaturated. If the solid skeleton of concrete is assumed to be rigid, research results have shown that the main transport mechanisms in an unsaturated porous material are advection of liquid-water and vapor diffusion (Mainguy *et al.*, 2001; Zhang *et al.*, 2015 & 2016). The main state of moisture in the porous material is mainly in liquid form. Thus, the mass balance equation can be written as:

$$\frac{\partial S \phi \rho_l}{\partial t} = \nabla(w_l + w_v) \tag{1}$$

where the flux of liquid w_l can be expressed by the extended Darcy's law with the liquid pressure P_l (Pa) as the driving potential

$$w_l = -\rho_l \frac{K_0 k_{rl}(S)}{\eta} \nabla P_l \tag{2}$$

and the flux of vapor diffusion is written as

$$w_v = -D_{v0} f(S, \phi) \nabla \rho_v \tag{3}$$

where S represents the degree of saturation, ρ_l (kg·m³) is the density of liquid phase, ϕ is the porosity of the porous material, k_{rl} is the relative permeability, η (Kg·m⁻¹·s⁻¹) is the liquid-water dynamic viscosity, K_0 (m²) is the intrinsic permeability to liquid-water, which is considered to be only related to the pore structure of the material, ρ_v is vapor density and D_{v0} (m²·s⁻¹) is the free vapor diffusion coefficient in the air.

The thermodynamic equilibrium between the liquid and vapor is assumed in this model. The water vapor sorption isotherm is formulized by the well-known van Genuchten (VG) equation (van Genuchten, 1980) which can provide a better fitting of measured data but with fewer parameters than the other equations (Zhang *et al.*, 2014).

$$P_c(S) = \alpha \left(S^{-1/m} - 1\right)^{1-m} \tag{4}$$

where P_c (Pa) is the macroscopic capillary pressure. α (Pa) and m are two parameters that should be determined by fitting the measured sorption isotherm.

The determination of the transport and material properties ($f(S, \phi)$ and k_{rl}) can be found in Zhang *et al.* (2015 & 2016).

2.2 Ion transport

The transport of various ions present in the porous materials by diffusion under the concentration gradient, advection with the flow of pore solution and migration under the electrical field is described by the extended Nernst-Planck equation (e.g., Baroghel-Bouny *et al.*, 2011; Jensen *et al.*, 2014).

$$\frac{\partial c_i}{\partial t} = \nabla \left(D_i \nabla c_i + z_i \frac{D_i}{RT} F c_i \nabla \psi\right) + v_l \nabla c_i + R_i \tag{5}$$

where z_i (-) is the charge number, and i represents the ith ion in the pore solution. F is the Faraday constant (9.64846e-4 C/mol). ψ (V) is the local electrical potential. v_i (m/s) is the liquid water velocity, which is provided by the moisture transport model. R_i is the source/sink term which can be used to take into account dissolution/precipitation determined by the chemical equilibrium.

The effective diffusion coefficient D_i (m²/s) is affected by the geometry of pore network and it is reasonable to assume that this effect is the same for all ionic species. D_i is described as the function of the tortuosity τ (-) and constructivity δ_i (-) of the pore structure (Atkinson *et al.*, 1984).

$$D_i = D_i^0 \frac{\phi \delta_i}{\tau^2} \tag{6}$$

where D_i^0 (m²/s) is the free diffusion coefficient of species i in pure water. δ_i is species dependent and related to the interaction between species and pore structure.

Poisson's equation is coupled with Eq. (5) to take into account the effect of the electrical potential on the ion transport in unsaturated porous media.

$$\nabla \psi = \frac{F}{\varepsilon} \sum c_i z_i \tag{7}$$

where ε is the dielectric permittivity of the liquid phase and considered equal to the relative permittivity ε_r of pure water times the vacuum permittivity ε_0=8.854e-12 C/V/m.

A variety of types of ionic species in the pore solution can be adsorbed on the surface of C-S-H, in particular chlorides for concrete. Ion binding can be represented by the surface complexation approach (physical adsorption) and the ion exchange reaction approach (chemical binding). Baroghel-Bouny *et al.* (2012) compared five methods to determine the chloride binding isotherms and found that all methods excellently agree with each other. Here we choose one of these models to implement into the mass transport models. If assuming equilibrium bonding, a Freundlich's type description can be used for physical adsorption of chlorides on to C-S-H and instantaneous Friedel's salt formation is suitable for chemical binding.

$$s_{Cl} = s_{Cl}^{p} + s_{Cl}^{c} = \mu c_{Cl^-}^{\gamma} + \delta n_{C_3A} \tag{8}$$

The flux boundary condition (also known as convective condition) is used to account for an imperfect moisture transport between the environment and the surface of the material. Dirichlet boundary condition is used for ion transport model.

3.0 EFFECT OF HETEROGENEITY ON TRANSPORT PROPERTIES

When modelling moisture transport in cementitious materials, most studies assume that the material is homogeneous (e.g., Mainguy *et al.*, 2001; Zhang *et al.*, 2015 & 2016); thus, a single porosity is used for the whole simulation domain. This simplification is generally acceptable for macroscopic scale simulations, but at the microscopic level, any aggregates or non-uniform distribution of hydration products may result in heterogeneity of the porous material. The method to consider the heterogeneity in the present study is presented as follows.

3.1 Porosity distribution from SEM-BSE image

As mentioned in the Introduction, a high simulation resolution always needs a small simulation domain. To reach a compromise between the size of the domain and the simulation resolution, a porosity distribution method is introduced in this study. The porosity distribution for a 2D domain is converted from an SEM-BSE image. The coarse aggregates are considered less impermeable than the mortar matrix (cement paste and fine aggregates), and at each pixel, the mortar matrix (including pores) is treated as homogeneous.

To apply this method, an SEM-BSE image must be taken on the mortar sample only with crushed limestone as aggregates to be sure that all aggregates have the same gray level under the BSE detector. Prior to imaging, the sample must be impregnated in the epoxy resin. Under the BSE detector, the low/impermeable materials are much brighter (aggregates and steel) than the cement paste, and pores are dark because of the presence of

epoxy in the empty space, so that the region with more pores is darker than the region with fewer pores. Therefore, the relationship between the gray level of the SEM-BSE image and the porosity can be established by assuming that they obey an exponential function (the S-shaped curve).

$$\phi(x, y) = a_1 + a_2 \exp\left[a_3 r(x, y)\right] \tag{9}$$

where $r(x, y)$ represents the normalized gray level at each pixel. a_1, a_2 and a_3 are three parameters.

The calculated porosity is limited to the range of $[\phi_l, \phi_h]$, and the corresponding gray level is in the range $[r_h, r_l]$ (h and l are the high and low boundaries, respectively). Substituting the lower and upper boundaries into the above equation, a_2 and a_3 can be calculated.

$$a_2 = \frac{\phi_h - a_1}{\exp\left(a_3 r_l\right)}$$
$$a_3 = \frac{1}{r_l - r_h} \ln \frac{a_1 - \phi_h}{a_1 - \phi_l} \tag{10}$$

The only unknown in these equations is a_1, which will be used to adjust the shape of the curve to fit the measured bulk porosity. The dependence of the shape of the curve on a_1 is shown in Fig.1. It is clear that a negative a_1 provides a convex downward curve and a positive a_1 shows a convex upward curve.
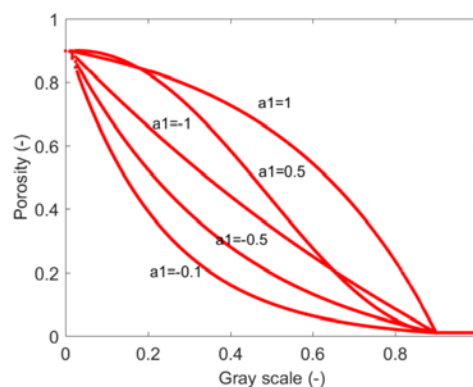

Fig. 1. Exponential function showing how to convert the gray level into porosity.

An example of calculated porosity is shown in Fig. 2. The mortar sample was made from ordinary Portland cement (OPC) with water-to-cement (w/c) ratio 0.5. A steel tube was horizontally cast in the sample. The region shown in Fig. 2a is below the steel tube, so that a clear water-bleeding zone shows in much dark color close to the steel tube. Aggregates, in much bright color, are randomly distributed in the mortar. Correspondingly, the calculated porosity in Fig. 2b shows that the water-bleeding zone has much high porosity, while the aggregates have low porosity. For some aggregates, such as number 4, 5 and 6, a region with high porosity around them can be seen.

In the example in Fig. 2, the lower and upper boundaries are given: gray level $r \subseteq [0.9, 0.01]$ and corresponding porosity$\phi \subseteq [0.01, 0.9]$. The measured bulk porosity for cement paste with 0.5 w/c is in the range of 0.35 - 0.40 (by means of the mass difference between saturated and 105°C dried states). By adjusting the value of a_1 in Eq. (10), we are able to fit the measured porosity (the impermeable aggregates and steel are excluded in the calculation). Finally, a_1=1.5 was used to calculate the porosity.

(a)

(b)
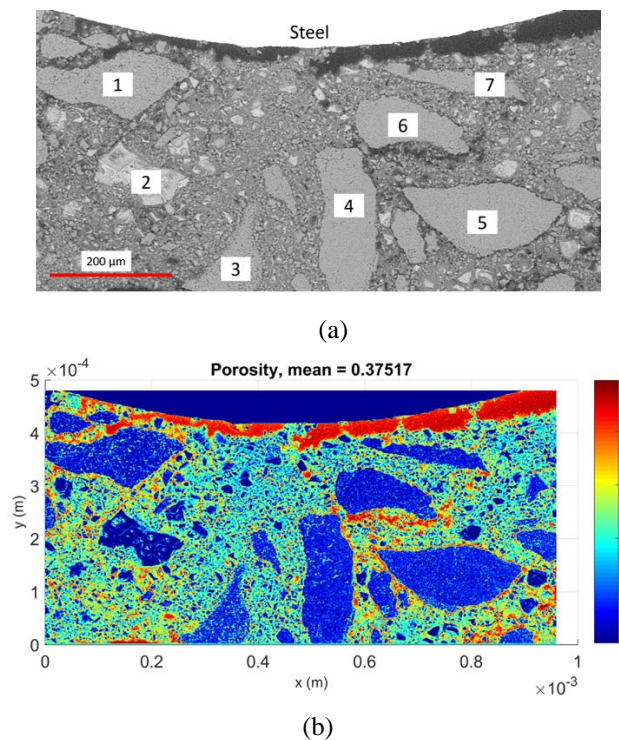
Fig. 2. An example of calculating porosity (b) based on the SEM-BSE image (a).

3.2 Sorption isotherm

In the mass transport model described above, several factors are primarily associated with porosity, such as sorption isotherms, resistance factor, intrinsic permeability, and ion diffusion coefficient (through tortuosity). When considering the porosity in the equation of sorption isotherms, we have the general form $S = f(RH, \phi)$.

The effect of porosity can be taken into account through one of the two parameters in the VG equation (see Eq. (4)). In the literature, the sorption isotherms (only desorption isotherm is considered in this study) for cementitious materials with different porosities were reported (e.g., Baroghel-Bouny, 2007). By fitting the measured sorption isotherms, we found that values of m are in a small range [0.4, 0.5] for OPC pastes. To simplify the model, m in VG equation is fixed to 0.45. Actually, this simplification does not reduce the accuracy of fitted sorption isotherms (see Fig. 4). The following equation is proposed to calculate α in the VG equation.

$$\alpha = c_1 e^{c_2 \phi} \qquad (11)$$

For isotherms reported in Baroghel-Bouny (2007), the parameters c_1 and c_2 are 154.37 MPa and -4.33, respectively. The exponential function with the negative c_2 can provide a downward curve (see Fig. 3).
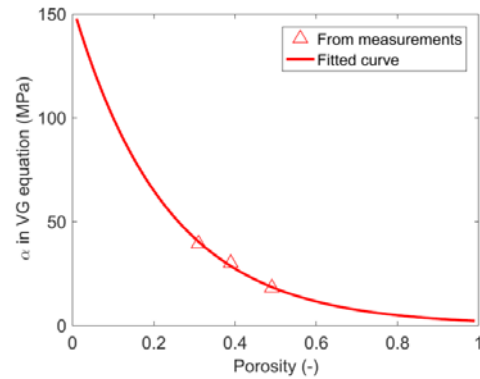

Fig. 3. The fitted $\alpha - \phi$ curve by Eq. (11) based on the measured desorption isotherms.

The calculated porosity-dependent desorption isotherms are shown in Fig. 4. For materials with high porosity, the curve slowly increases initially and dramatically jumps at high RH. For materials with low porosity, the curve suddenly increases at the beginning and rises gently later on. The proposed calculation method cannot be validated for the whole range of porosity (from 0 to 1) due to the limit data available data in the literature, but it is supposed to be theoretically correct for materials with different porosities.
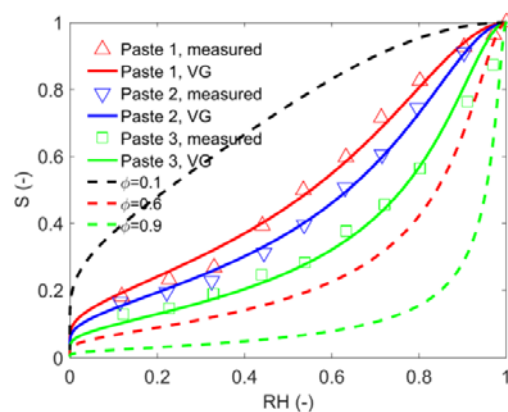

Fig. 4. The fitted desorption isotherms by VG equation (measured curves taken from Baroghel-Bouny, 2007) and extrapolated desorption curves for materials with different porosities.

3.3 Effect of porosity on transport properties

In the present moisture transport model, heterogeneity is taken into account through the porosity which directly affects the resistance factor$f(S, \phi)$. For advection of liquid, as previously stated, the intrinsic permeability K_0 is solely

dependent on the microstructure of the material; that is porosity. Therefore, K_0 can be written as a function of porosity $K_0(\phi)$.

To establish a relationship between permeability and porosity, the Kozeny–Carman (KC) equation can be used. Considering that the flow in one-size straight tubes obeys the Navier–Stokes (N-S) equations, Hagen–Poiseuille equation is an exact solution to the N-S equations. Meanwhile, Darcy's law can give the flux through these tubes. The comparison of Hagen–Poiseuille equation with Darcy's law yields water permeability K_0 as a function of porosity ϕ, the specific surface area S (m²/kg), and tortuosity τ.

$$K_0 = \frac{\phi^3}{C_K \tau^2 \rho_S^2} \tag{12}$$

where C_K is KC coefficient. In the present study, we let C_K as a free parameter that is adjustable to fit the measured intrinsic permeability. Tortuosity τ in Eq. (11) is still unknown.

3.4 Tortuosity effect

The tortuosity τ is given as the ratio between the average length of the pathway (L_e) that water molecules or ions move within two locations and the straight distance of these two locations (normally, the thickness of the sample, L).

$$\tau = \frac{L_e}{L} \tag{13}$$

It is clear that $1/\tau$ should be always smaller than 1. Primarily, we can assume that tortuosity is a function of porosity, as that pores in the region with higher porosity should be better connected and have fewer restrictions on moisture and ion transport. The traditional Bruggeman relation is one commonly used relation.

$$\tau = \phi^{b_1} \tag{14}$$

By examining a variety of equations for $\phi - \tau$ relation, including Eq. (14), Matyka *et al.* (2008) found that the relation $\tau - 1 \sim \ln \phi$ proposed by Boudreau and Meysman (2006) can provide a good agreement with numerical results for muds, and the function is written as

$$\tau = 1 - b_2 \ln \phi \tag{15}$$

To check these functions for tortuosity, experimental data are taken from Promentilla *et al.*, (2009) in which tortuosity was calculated based on the 3D microstructure measured by X-ray computed tomography. The best fitted results by Eqs. (14) and (15) are shown in Figure 5. It is clear that when porosity is below the value of about 0.20, the tortuosity exhibited a significant and sudden increase. This seems to be consistent with the experimental results of Powers *et al.* (1959) on water permeability measurements. They suggest that the capillary pores in cement pastes exhibit a percolation transition from connected to disconnected phase at a porosity of about 0.20, wherein a sharp decrease of permeability

is observed. For hardened cement pastes, τ is significantly larger than that for the other porous materials in the range of low porosity that is why most proposed equations (e.g., Eq. (15)) are not suitable for cementitious materials.
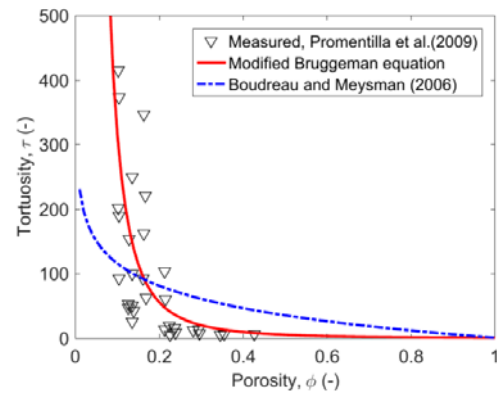

Fig. 5. Comparison of measured and calculated tortuosity for hardened cement pastes with w/c=0.5. Fitted b_1 in Eq. (14) is 2.5 and b_2 in Eq. (15) is 50.

To calculate K_0 at each pixel, C_K must be determined. We take the measured K_0 for the bulk cementitious materials to inversely determine C_K in Eq. (12). Unfortunately, no such measurements have done for the mortar sample reported in Fig. 2. Previous study (Zhang *et al.*, 2016) reviewed the measured K_0 in the literature and concluded that for cementitious materials (regardless of pastes or concretes) with w/c between 0.4 and 0.5 have K_0 in the order of magnitude of 10^{-21} m². It is acceptable to assume that K_0 for the mortar sample reported in Fig. 2 is in the same order of magnitude and then C_K can be inversely calculated.
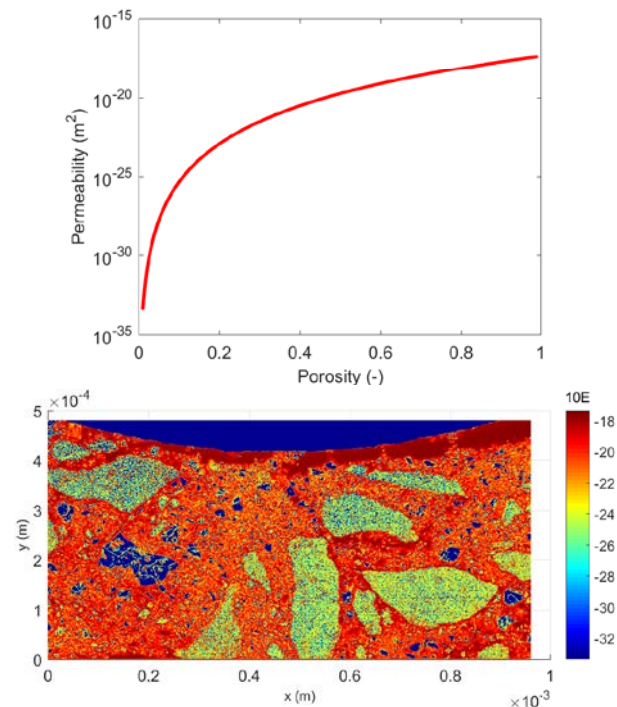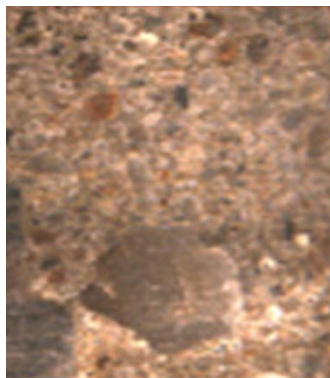

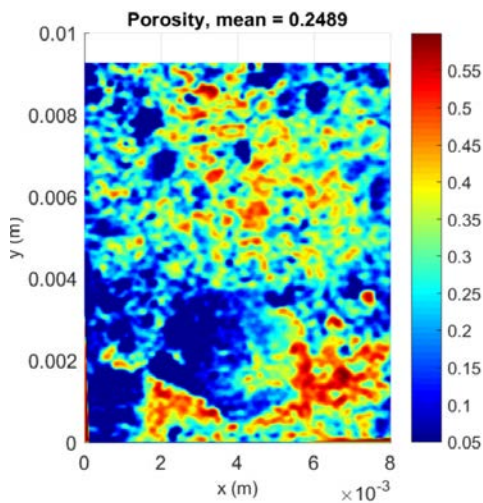**Fig. 6.** Permeability calculated by KC equation.

Results of K_0 calculated by the KC equation at each pixel in Fig. 6 show a much wide range of K_0 that the water-bleeding zone has much high K_0 (over 10^{-18} m²) and the low permeable regions have K_0 below 10^{-30} m². The limestone aggregates have K_0 around 10^{-24} m², which is 1000 times as low as the average permeability over the whole domain.

4.0 EXPERIMENTAL CALIBRATION ON CHLORIDES TRANSPORT

In the literature, moisture content and ion concentration (mainly chloride) are rarely experimentally mapped on the mesoscale which the present study is focused on. This is mainly due to the difficulty to conduct such measurements on a very small scale by using the traditional methods (e.g., RH sensor for moisture and AgNO₃ titration method for chloride concentration). Therefore, we do not attempt to verify both moisture and ion transport models in this study. We will only focus on the verification of the proposed local homogenization method and its effect on the chloride transport since the presence of chlorides is directly related to the degradation of reinforced concrete structures.
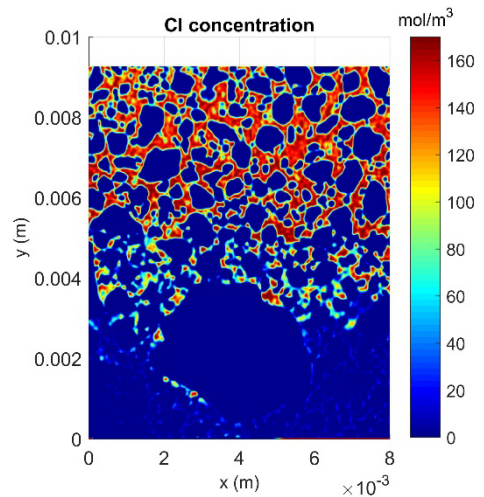
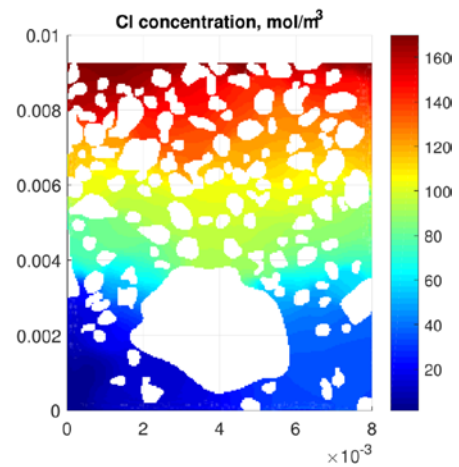Experimental data are taken from the literature (Moradllo *et al.*, 2017), in which micro X-ray fluorescence (μXRF) was used to image chloride concentration on mortar samples. The resolution of μXRF is about 50 μm and thus it can measure a domain having size in centimetre. The OPC mortar sample was cured in limewater for two weeks and then one face was exposed to an aqueous sodium chloride solution for 45 days at room temperature. Prior to μXRF tests, the sample was split along the direction of ion penetration and the fracture face was polished with 120 grit sandpaper to create a flat surface. One advantage of μXRF techniques is that it does not need extremely flat surface which is generally required for the quantitative analysis of energy dispersive X-ray spectroscopy (EDX).

The raw data from μXRF is the number of fluoresced X-rays collected in a certain energy window, which also includes background signal. To determine chloride concentration, reference tests must be done by analysing the sample with known amount of chlorides. Unfortunately, the authors of (Moradllo et

(a)

(a)

(b)

Fig. 7. The selected simulation domain (a: optical image; b: calculated porosity).

(b)

Fig. 8. The measured (a) and simulated (b) Cl concentration map.

al., 2017) did not image the sample under the BSE detector and only provided the images taken in an optical microscope, which are not ideal for the verification of the method proposed in this study. However, to the best of our knowledge, data in Moradllo *et al.* (2017) are most suitable ones that can be found in the literature for our purpose.

In this study, a domain with size about 8 mm × 9 mm is chosen (see Fig. 7a). By using the proposed method, the porosity distribution can be calculated as shown in Fig. 7b. The regions with extremely low porosity (in blue) are occupied by aggregates, while the regions with red color have more pores. Fig. 8a shows the measured Cl concentration, in which the aggregates were removed from the matrix. Comparing Fig. 8a with Fig. 7b, we observe that the locations of some aggregates do not match very well. This is mainly due to the fact that it is difficult to distinguish aggregates from cement pastes because the color scale of them in an optical image is not significantly different. To reduce the effect of the imperfect data, we used the measured Cl concentration image (Fig. 8a) to create the geometry and then added the calculated porosity (Fig. 7b) to the geometry for simulations. Therefore, aggregates were excluded from simulations.

Four ions are considered in the simulations: Cl^-, OH^-, Na^+, and K^+. Initially, the mortar sample is saturated, so that pores are filled with the pore solution. The corresponding ion concentrations for the same type of OPC are: 0, 180.2, 87.2, and 93 mol/m^3 (Zhang and Scherer, 2017). At the upper boundary, the concentration of Cl^- and Na^+ is set as 170 mol/m^3 according to the experimental condition.
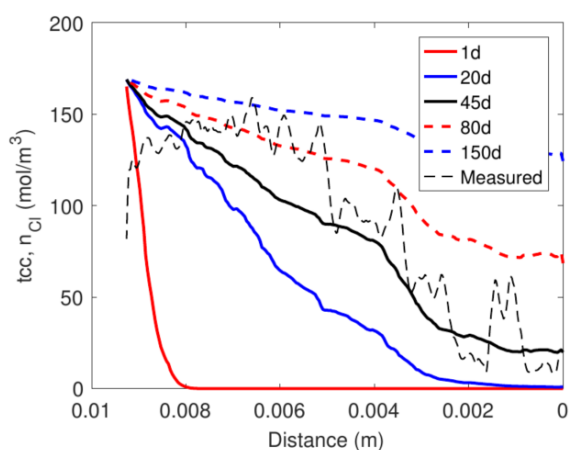

Fig. 9. Comparison of measured (excluding aggregates) and simulated Cl concentration profiles.

The measured Cl concentration in Figs. 8 and 9 clearly shows three regions: high Cl concentration in the region from top to about 0.005 m, Cl concentration decreasing region between 0.002 and 0.005 m and low Cl concentration in the deep region. This general trend is captured in the simulated results (see the black solid curve in Fig. 9). Some details in the

simulated results are different to the measured ones. For instance, the high measured Cl concentration can be seen under the largest aggregate in Fig. 8, but simulated results do not show this. One reason is that the calculated porosity in Fig. 7b does not show a clear path around this aggregate for the Cl transport.

5.0   CONCLUSIONS

In this study, an image-based local homogenization method is proposed based on the experimental SEM-BSE image. Comparing with the imperfect data (optical image and measured Cl concentration in 2D) taken from the literature, the general trend of chlorides transport and concentration distribution can be captured by the proposed method but some details are different.

To further calibrated the proposed method, a set of experimental data, including SEM-BSE images, moisture distribution and ion concentration, are needed. Similar measurements of iron concentration are also desirable, as the proposed method will be applied to modelling the precipitation and growth of corrosion products and corrosion-induced cracking.

References

Abyaneh, S. D., Wong, H., Buenfeld, N., 2013. Modelling the diffusivity of mortar and concrete using a three- dimensional mesostructure with several aggregate shapes, Computational Materials Science 78, 63–73.

Angst, U. M., Geiker, M. R., Michel, A., Gehlen, C., Wong, H., Isgor, O. B., Elsener, B., Hansson, C. M., Francois, R., Hornbostel, K., Polder, R., Alonso, M. C., Sanchez, M., Correia, M. J., Criado, M., Sagues, A., Buenfeld, N., 2017. The steel–concrete interface, Materials and Structures 50 (2) 143.

Atkinson, A., Nickerson, A.K., 1984. The diffusion of ions through water-saturated cement, Journal of Materials Science 19, 3068–3078.

Baroghel-Bouny, V., Thiery, M., Wang, X., 2011. Modelling of isothermal coupled moisture-ion transport in cementitious materials, Cement and Concrete Research 41, 828–841.

Baroghel-Bouny, V., Wang, X., Thiery, M., Saillio, M., Barberon, F., 2012. Prediction of chloride binding isotherms of cementitious materials by analytical model or numerical inverse analysis, Cement and Concrete Research 42, 1207–1224.

Baroghel-Bouny, V., 2007. Water vapour sorption experiments on hardened cementitious materials. Part II: Essential tool for assessment of transport

properties and for durability prediction, Cement and Concrete Research 37, 438–454.

Boudreau, B. P., Meysman, F. J., 2006. Predicted tortuosity of muds. Geology, 34(8), 693-696.

Du, X., Jin, L., Ma, G., 2014. A meso-scale numerical method for the simulation of chloride diffusivity in concrete, Finite Elements in Analysis and Design 85, 87–100.

Horne, A.T., Richardson, I.G. & Brydson, R.M.D., 2007. Quantitative analysis of the microstructure of interfaces in steel reinforced concrete. Cement and Concrete Research, 37(12), 1613–1623.

Jensen, M.M., Johannesson, B., Geiker, M.R., 2014. Framework for reactive mass transport: Phase change modelling of concrete by a coupled mass transport and chemical equilibrium model, Computational Materials Science 92, 213-223.

Mainguy, M., Coussy, O., Baroghel-Bouny, V., 2001. Role of air pressure in drying of weakly permeable materials, Journal of Engineering Mechanics 127, 582–592.

Matyka, M., Khalili, A., Koza, Z., 2008. Tortuosity-porosity relation in porous media flow, Physical Review E 78 (2) 026306.

Moradllo, M. K., Sudbrink, B., Hu, Q., Aboustait, M., Tabb, B., Ley, M. T., & Davis, J. M., 2017. Using micro X-ray fluorescence to image chloride profiles in concrete. Cement and Concrete Research, 92, 128-141.

Powers, T. C., Copeland, L. E., Mann, H., 1959. Capillary continuity or discontinuity in cement pastes, Portland Cement Bullet 110, 3–12.

Promentilla, M. A. B., Sugiyama, T., Hitomi, T., Takeda, N., 2009. Quantification of tortuosity in hardened cement pastes using synchrotron-based x-ray computed microtomography, Cement and Concrete Research 39 (6) 548–557.

Van Genuchten, M.T., 1980. A closed-form equation for predicting the hydraulic conductivity of unsaturated soils, Soil Science, 44, 892-898.

Wong, H. S., Zhao, Y. X., Karimi, A. R., Buenfeld, N. R., Jin, W. L., 2010. On the penetration of corrosion products from reinforcing steel into concrete due to chloride-induced corrosion, Corrosion Science 52 (7) 2469–2480.

Zhang, Z., Thiéry, M. and Baroghel-Bouny, V., 2014. A review and statistical study of existing hysteresis models for cementitious materials. Cement and concrete research, 57, 44-60.

Zhang, Z., Thiery, M., Baroghel-Bouny, V., 2015. Numerical modelling of moisture transfers with hysteresis within cementitious materials: Verification and investigation of the effects of repeated wetting–drying boundary conditions, Cement and Concrete Research 68, 10–23.

Zhang, Z., Thiery, M., Baroghel-Bouny, V., 2016. Investigation of moisture transport properties of cementitious materials, Cement and Concrete Research 89, 257–268.

Zhang, Z., Scherer, G. W., 2017. Supercritical drying of cementitious materials, Cement and Concrete Research 99, 137–154.

Zhao, Y., Zhang, X., Jin, W., 2017. Influence of environment on the development of corrosion product-filled paste and a corrosion layer at the steel/concrete interface, Corrosion Science 124, 1-9.